Supporting Information

Size-Tunable Hemoglobin Oxygen Carriers with Antioxidant and Pro-Angiogenic Functions for Wound Healing

Yu Zhang[a], Honglei Zhu[a], Qinqi Wang[a], Leijiao Li[a,], Liana Shestakova[b], Youry Ostrovsky[b], Xincui Shi[a], Yuan Cui[a,]* and Wenliang Li[a,]**

1. Materials

Bovine hemoglobin (Hb), Bovine hemoglobin ($MnSO_4$), ammonium bicarbonate (NH_4HCO_3), anhydrous manganese chloride ($MnCl_2$), sodium carbonate (Na_2CO_3), glutaraldehyde ($C_5H_8O_2$), human albumin (HSA), ethylenediaminetetraacetic acid (EDTA), sodium hydroxide (NaOH), caffeic acid (CA), 1-ethyl-(3-dimethylaminopropyl)carbodiimide (EDC), N-hydroxysuccinimide (NHS), glutathione (GSH), 1,1-diphenyl-2-picrylhydrazyl (DPPH), 2,2'-azino-bis(3-ethlbenzothiazoline-6-sulfonic acid) diammonium salt (ABTS) purchased from Aladdin Reagent (Shanghai) Co., Ltd. Healthy male C57BL/6J rat weighing about 180-220 g (SPF grade, 6-8 weeks old) from Liaoning Changsheng Biotechnology Co., Ltd. All animal experiments, including animal care, dosing, and termination, were performed according to the guidelines of the local Animal Ethics Committee of Changchun University of Science and Technology (registration number: 202524).

2. Experimental Section

2.1 Synthesis of S-Hb

The small-sized hemoglobin nanoparticles (S-Hb) were synthesized *via* a co-precipitation method. Briefly, 0.5 M $MnCl_2$ solution containing Hb was mixed with 0.25 M Na_2CO_3 under stirring for 5 min. Subsequently, 1 mL of 20% HSA solution was added immediately, followed by another 5 min of incubation. The mixture was centrifuged at 3000×g for 3 min, and the precipitate was washed with ultrapure water 2-3 times. The obtained precipitate was resuspended in 20 mL of water, followed by the addition of 20 mL of aqueous solution containing 32 μL of glutaraldehyde. The mixture was shaken for 1 h for cross-linking. After centrifugation and washing, the particles were resuspended in 40 mL of 0.5 M EDTA solution and shaken for 0.5 h to remove the $MnCO_3$ templates. Finally, 1 mL of freshly prepared

$NaBH_4$ solution (10 mg/mL) was added and reacted for 0.5 h. The resulting S-Hb were collected by centrifugation at 10000×g, washed, and stored at 4 °C in the dark. The XRD patterns of S-Hb at different preparation stages is displayed in Fig. S1 (a-c) and the surface chemical composition and elemental analysis of S-Hb is displayed in Fig. S2 (a-f).

2.2 Synthesis of L-Hb

The large-sized hemoglobin microparticles (L-Hb) were prepared using a modified template method. Specifically, a seed solution containing 4 mg $MnSO_4$ and 0.1 mg NH_4HCO_3 was added into 0.016 M $MnSO_4$ solution containing 500 mg Hb. Under ultrasonication, 10 mL of ethanol was rapidly added (10 s), followed by the quick addition of 0.16 M NH_4HCO_3 solution (30 s). The mixture was stirred at 4 °C for 1 h. The Hb-$MnCO_3$ intermediate particles were collected by centrifugation (3000×g, 3 min) and washed with water. To prevent Hb dissociation, the particles were cross-linked in 20 mL of 0.025% glutaraldehyde for 1 h. After washing, the precipitate was resuspended in 0.1 M EDTA solution (pH 7.4) and shaken for 0.5 h to dissolve the $MnCO_3$ templates. The final L-Hb were collected and stored at 4 °C for further use. The XRD patterns of L-Hb at different preparation stages is displayed in Fig. S1 (d-f) and the surface chemical composition and elemental analysis of L-Hb is displayed in Fig. S2 (g-l).

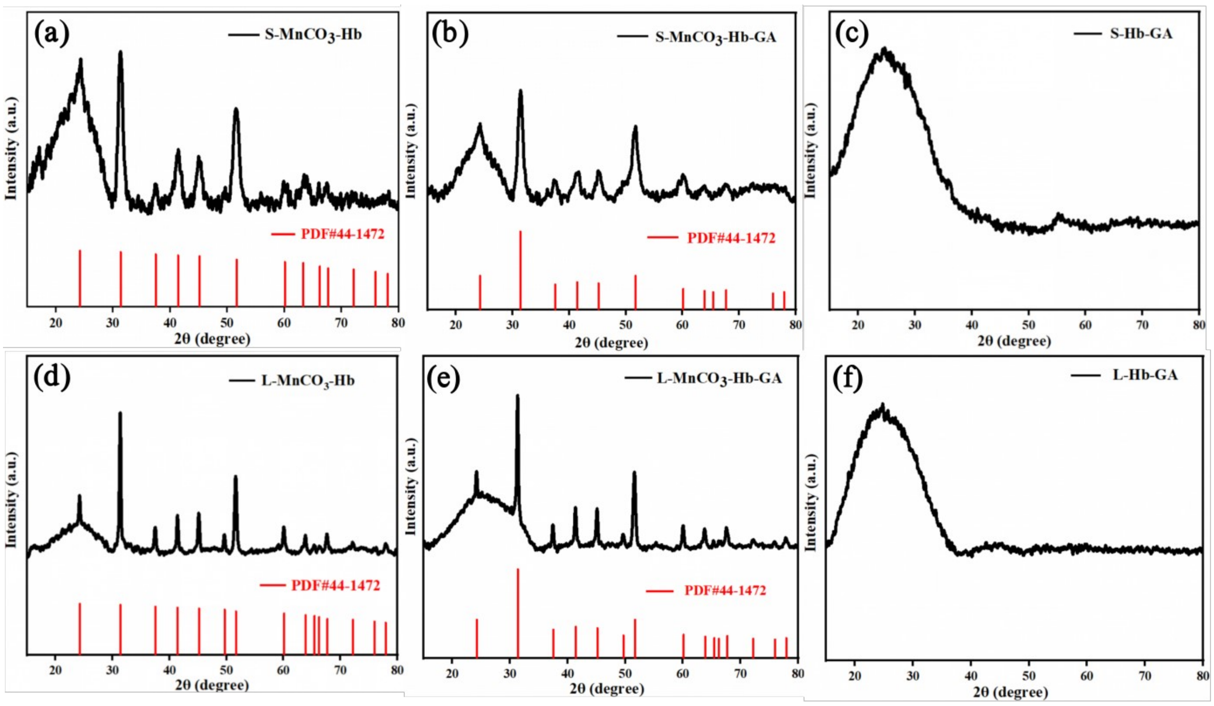

Fig. S1 XRD patterns of S-Hb and L-Hb at different preparation stages. (a-c) Nano-sized S-Hb and (d-f) micro-sized L-Hb: (a, d) $MnCO_3$-Hb composites; (b, e) $MnCO_3$-Hb-GA intermediates; (c, f) final GA-Hb scaffolds after template removal. The red lines represent the standard $MnCO_3$ card (JCPDS No. 44-1472).

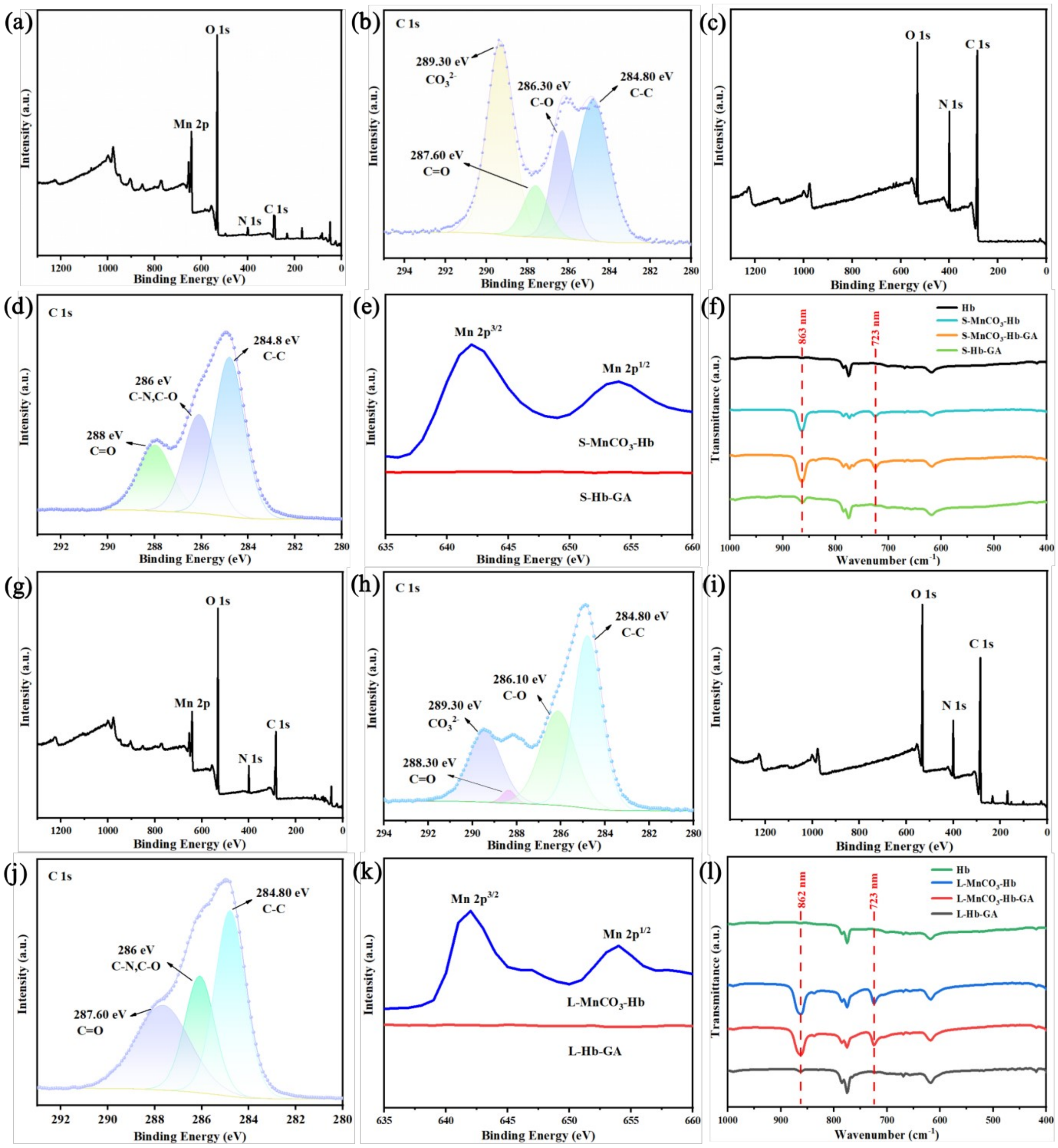

Fig. S2 Surface chemical composition and elemental analysis of size-tunable HBOCs. (a-f) Nano-sized S-Hb and (g-l) micro-sized L-Hb at different preparation stages: (a, g) XPS survey spectra of $MnCO_3$-Hb; (b, h) high-resolution C 1s spectra; (c, i) XPS survey spectra of the final GA-Hb scaffolds; (d, j) high-resolution C 1s spectra; (e, k) Mn 2p spectra; (f, l) FTIR spectra.

2.3 Confocal Microscopic Characterization of Glutaraldehyde-mediated Cross-linking

To visualize the cross-linking between glutaraldehyde (GA) and Hb, confocal laser scanning microscopy (CLSM) was employed for fluorescence analysis of products at different fabrication stages. During the process, GA cross-links with Hb *via* Schiff base reaction, which confers intrinsic green fluorescence to the resulting particles. As shown in Fig. S3, no discernible fluorescence signal was observed in the CLSM image of the intermediate product, $MnCO_3$-Hb, before GA cross-linking. In contrast, $MnCO_3$-Hb-GA, obtained after GA treatment, exhibited strong green fluorescence under dark-field conditions. This autofluorescence is attributed to the formation of the C=N conjugated structure via Schiff base reaction between the aldehyde groups of GA and the amino groups of Hb, confirming the successful cross-linking. Following the removal of the $MnCO_3$ templates, the final Hb-GA particles retained robust green fluorescence, with the fluorescence distribution matching the particle morphology observed in bright-field images perfectly. This indicates that the etching of the inorganic templates does not disrupt the conjugated cross-linking network between Hb and GA. Furthermore, the CLSM images demonstrated excellent dispersibility of the particles at each stage within the aqueous phase.

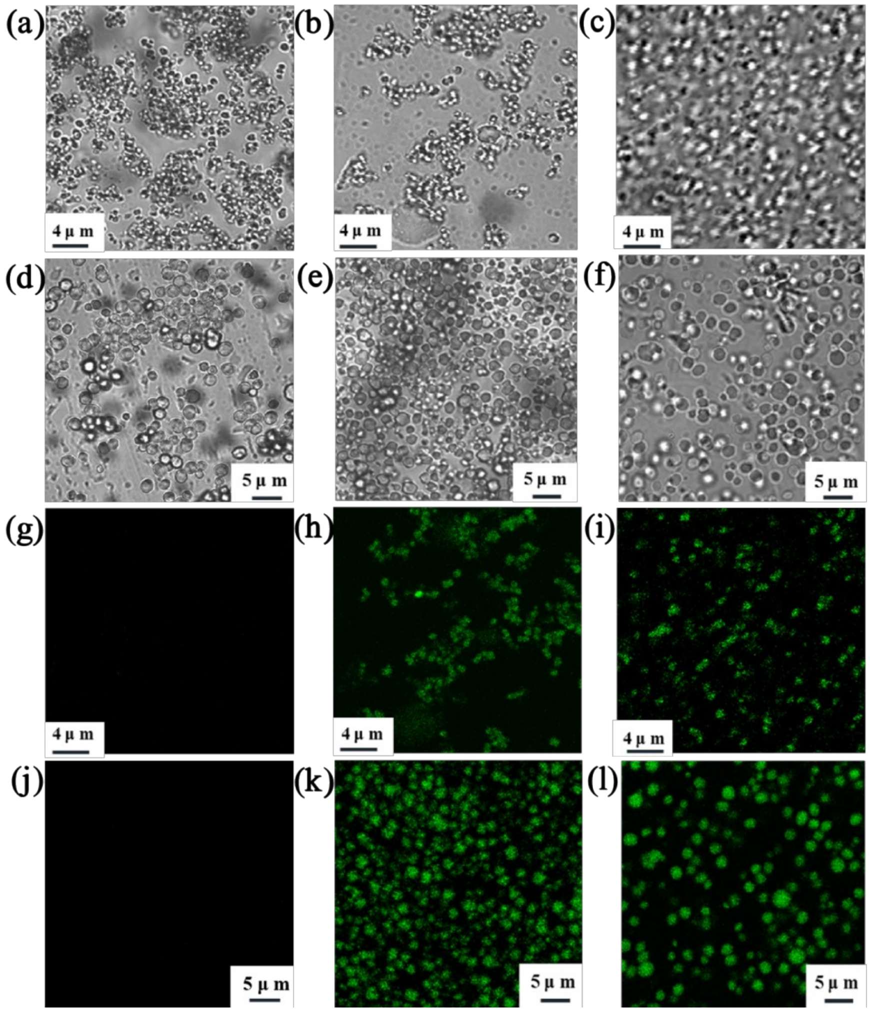

Fig. S3 CLSM characterization of Hb-based scaffolds. (a-f) Bright-field and (g-l) dark-field CLSM images of S-Hb-CA (top) and L-Hb-CA (bottom).

Imaging parameters: CLSM observations were performed using a CLSM 510 Meta (Carl Zeiss MicroImaging GmbH, Jena, Germany) equipped with a 100× oil immersion objective (numerical aperture 1.3). The excitation wavelength was set at 488 nm, and images were collected through a 505 nm long-pass emission filter.

2.4 Surface Charge Characterization

The modification of CA on the carrier surface was further confirmed by changes in surface charge. As shown in Fig. S4, the Zeta potential of Hb-CA nanoparticles decreased significantly from -4.7 mV to -37.2 mV after functionalization. A similar downward trend in surface potential was observed for both S-Hb-CA and L-Hb-CA. This is primarily attributed to the fact that the binding of CA molecules to the protein backbone significantly increases the negative charge density on the carrier surface. This resulting increase in surface negative charge not only validates the successful loading of CA but also enhances the colloidal stability of the particles in physiological media by strengthening electrostatic repulsion.

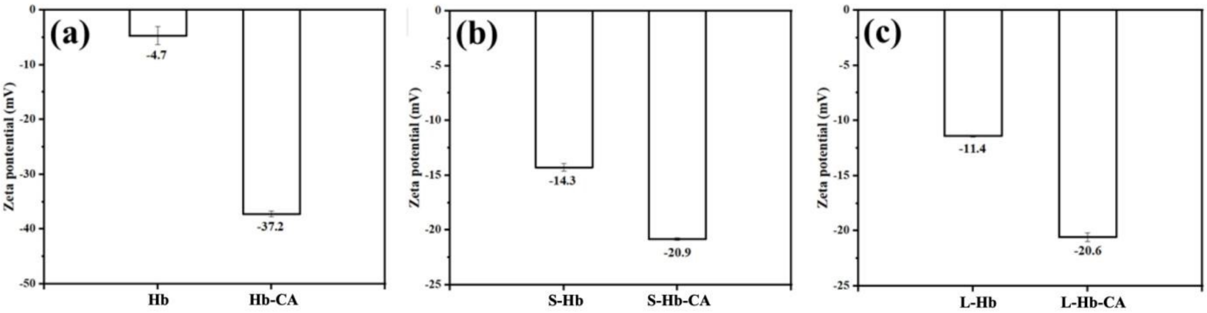

Fig. S4 Zeta potential analysis of HBOCs before and after CA functionalization. (a) Hb-CA, (b) S-Hb-CA, and (c) L-Hb-CA.

2.5 Determination of CA Loading Efficiency

The loading efficiency of CA was quantified using a standard calibration curve ($y = 0.0774x + 0.0058$, $R^2 = 0.9951$) established via UV-Vis spectroscopy (Fig. S5). Following the conjugation reaction, unreacted CA molecules were separated from the carriers. Hb-CA was purified by dialysis (MWCO: 3500 Da), while S-Hb-CA and L-Hb-CA was collected by centrifugation at 3000 × g for 3 min. The absorbance of the resulting supernatants was measured at 323 nm to determine the concentration of free CA. By comparing the amount of free CA with the initial input, the loading efficiencies for Hb-CA, S-Hb-CA, and L-Hb-CA were calculated to be 42.4%, 50.68%, and 65.96%, respectively.

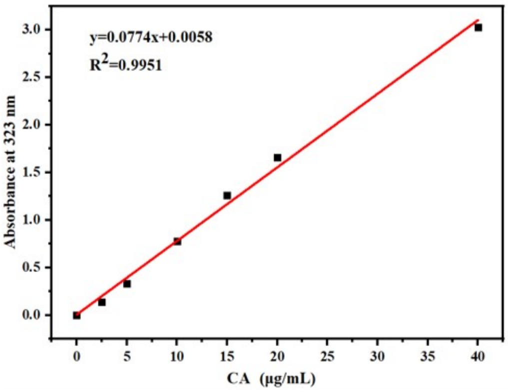

Fig. S5 Standard calibration curve of caffeic acid (CA) recorded at 323 nm.

2.6 Hydrodynamic Size Distribution and Colloidal Stability Evaluation

The hydrodynamic diameters of the three CA-modified carriers were characterized using dynamic light scattering (DLS). As illustrated in Fig. S6 (a-c), the average hydrodynamic sizes of Hb-CA, S-Hb-CA, and L-Hb-CA were approximately 11.29 nm, 571.14 nm, and 1.65 μm, respectively. Compared with the TEM observations prior to CA loading, the functionalization process caused no significant change in particle size, indicating that the composite systems maintain excellent monodispersity in the aqueous phase.

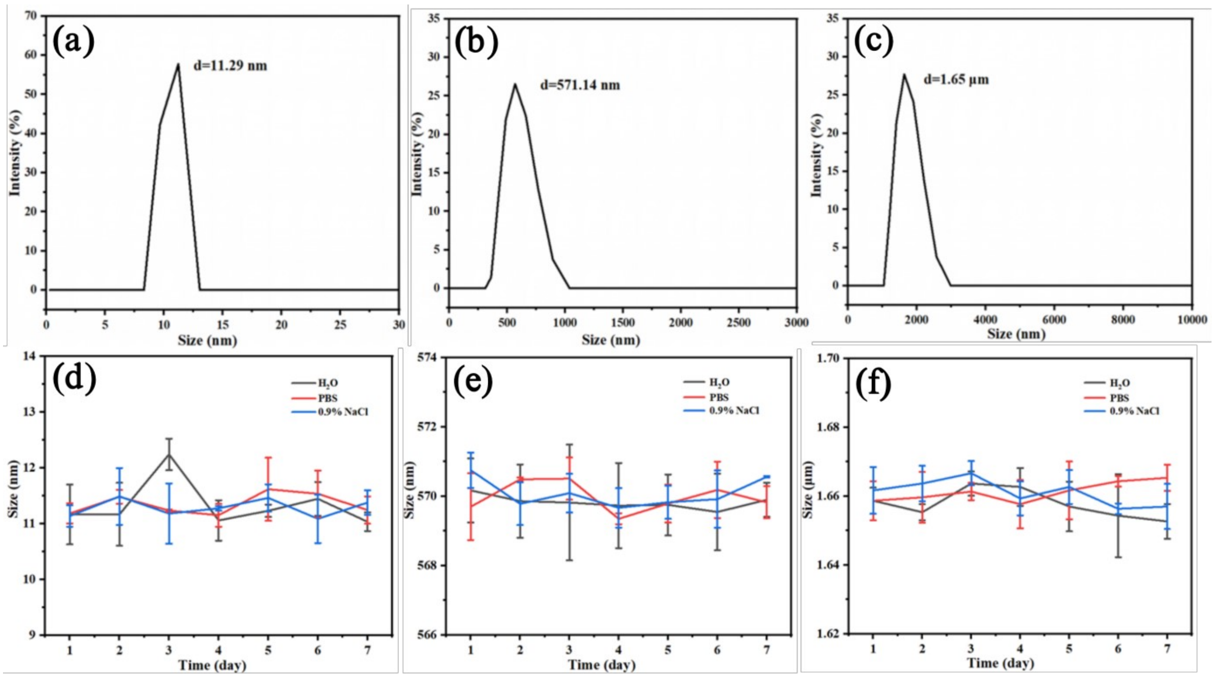

Fig. S6 Hydrodynamic size distribution and colloidal stability evaluation. (a-c) DLS size distribution of Hb-CA, S-Hb-CA, and L-Hb-CA. (d-f) Hydrodynamic diameter changes in deionized H_2O, PBS, and 0.9% NaCl over a 7-day storage period.

To evaluate the stability of these systems in various media, the time-dependent size changes of the three carriers were monitored in deionized water, phosphate-buffered saline

(PBS), and physiological saline (0.9% NaCl). As shown in Fig. S6 (d-f), the hydrodynamic diameters exhibited negligible fluctuations across all tested media over a 7-day observation period. These results demonstrate that both the nano-scale S-Hb-CA and micro-scale L-Hb-CA possess outstanding colloidal stability, providing a robust foundation for their further biomedical applications.

2.7 *In Vitro* cytotoxicity Assay and hemocompatibility Assessment

The *in vitro* cytotoxicity of HBOCs with different sizes was quantitatively evaluated using the MTT assay on L929 fibroblasts. This colorimetric assay relies on the reduction of yellow MTT reagent to purple formazan crystals by mitochondrial succinate dehydrogenase in viable cells; thus, the absorbance at 490 nm directly reflects cellular metabolic activity and proliferation. As shown in Fig. S7, L929 cells maintained high viability after 24 h of incubation with various concentrations of Hb-CA, S-Hb-CA, and L-Hb-CA. Within the tested range of 3.125-400 μg/mL, the relative cell viability remained consistently above 90%. Even at the highest concentration (400 μg/mL), no significant cytotoxicity was observed for any of the three carriers, demonstrating their excellent biocompatibility for further biomedical applications.

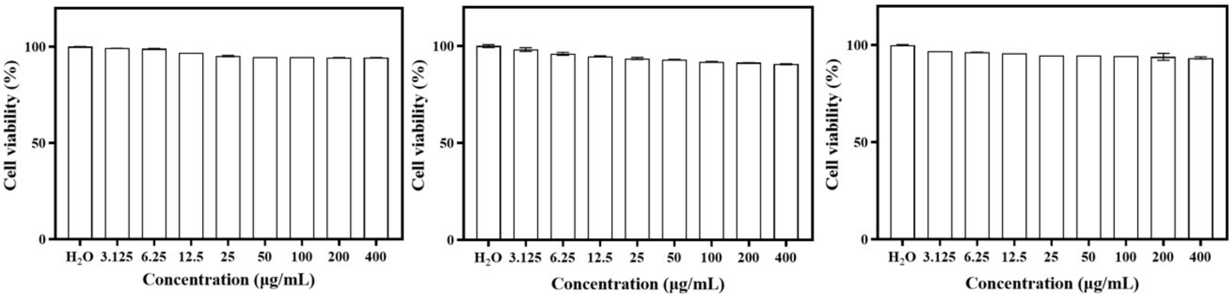

Fig. S7 *In vitro* cytotoxicity evaluation of size-tunable HBOCs. Cell viability of L929 fibroblasts after 24 h incubation with various concentrations (3.125-400 μg/mL) of (a) Hb-CA, (b) S-Hb-CA, and (c) L-Hb-CA, as determined by MTT assay (n=3).

The hemocompatibility of the HBOCs was systematically evaluated via a hemolysis assay using mouse red blood cells (RBCs), with deionized H_2O serving as the positive control (100% hemolysis). According to the UV-vis spectra (Fig. S8 (a-c)), the H_2O group exhibited a strong characteristic hemoglobin absorbance peak at 541 nm due to RBC rupture, whereas all experimental groups showed negligible absorbance across the entire concentration range. Quantitative analysis (Fig. S8 (d-f)) revealed that at the maximum concentration of 400 μg/mL, the hemolysis rates for Hb-CA, S-Hb-CA, and L-Hb-CA were 2.8%, 3.0%, and 1.7%, respectively, all well below the internationally accepted 5% safety threshold. Furthermore, the optical photographs of the supernatants (insets in Fig. S8) clearly show that the experimental groups remained colorless and transparent, in sharp contrast to the bright red supernatant of the positive control. These findings confirm the high biosafety and hemocompatibility of the developed materials.

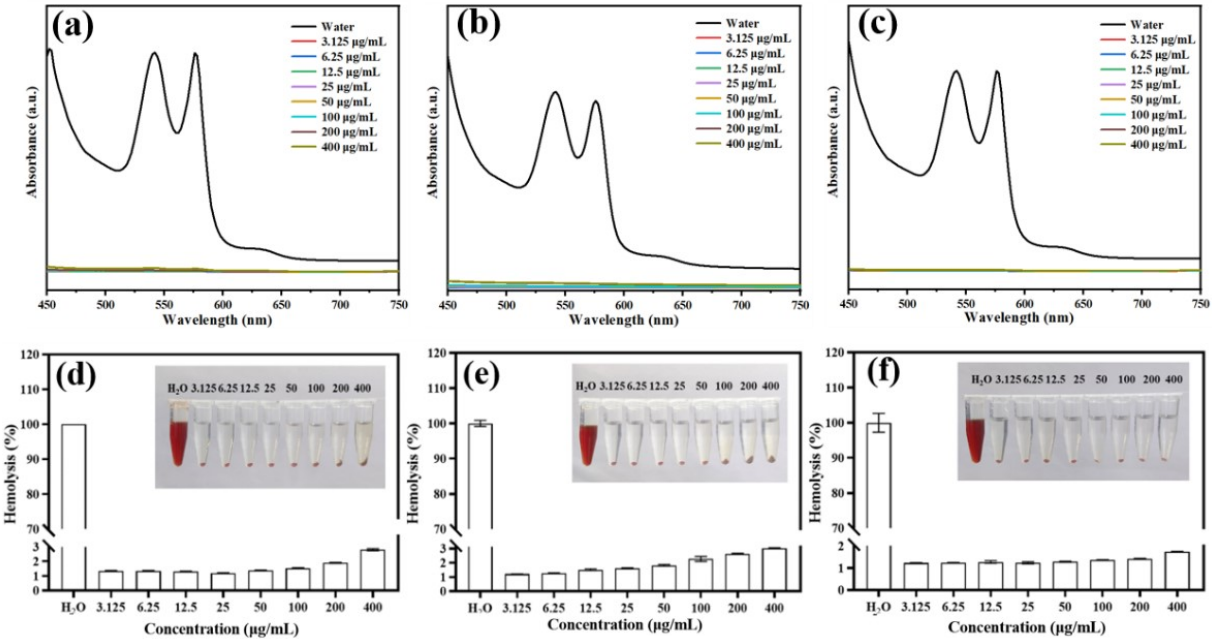

Fig. S8 Hemocompatibility assessment of various HBOCs. (a-c) UV-vis absorption spectra of supernatant after incubation with (a) Hb-CA, (b) S-Hb-CA, and (c) L-Hb-CA at different concentrations (3.125-400 μg/mL). (d-f) Quantitative hemolysis rates and corresponding optical photographs (insets) for (d) Hb-CA, (e) S-Hb-CA, and (f) L-Hb-CA. H_2O was used as the positive control. All groups remained below the 5% safety threshold.

2.8 Evaluation of *In Vivo* Wound Healing

The relative wound area at different stages was quantitatively analyzed using ImageJ software. As shown in Fig. S9, the wound closure rate for all treatment groups exhibited a distinct linear upward trend over time. By day 10, the PBS group still presented 11.01% of unhealed wound area with suboptimal recovery. In contrast, the relative wound area in the L-Hb-CA group decreased to 2.28%, representing a closure rate of 97.72% and nearly complete healing. These findings strongly demonstrate the superior advantages of micro-scale oxygen carriers in modulating the hypoxic wound microenvironment and accelerating tissue reconstruction.

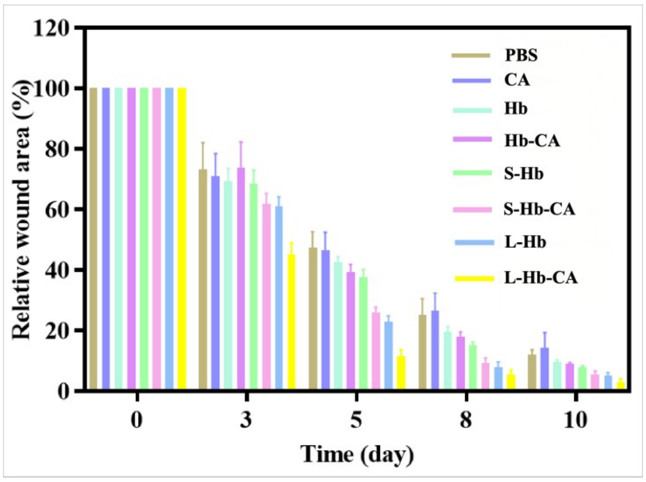

Fig. S9 Changes in wound area in mice during different treatment processes.

2.9 Systemic Safety and Histopathological Assessment

To systematically evaluate the long-term in vivo biosafety of the oxygen carriers, major organs (heart, liver, spleen, lungs, and kidney) were harvested for H&E staining and histopathological analysis. As illustrated in Fig. S10, no significant pathological damage was observed in the major metabolic and functional organs after 10 days of continuous administration. Specifically, no cell degeneration, inflammatory infiltration, or immune hyperplasia was detected in the heart, liver, or spleen tissues. The alveolar structures in the lungs remained intact, and the kidney tissues showed no signs of lesion. These histopathological findings confirm that the oxygen carriers exert no evident toxic side effects on major organs, demonstrating excellent *in vivo* biocompatibility.

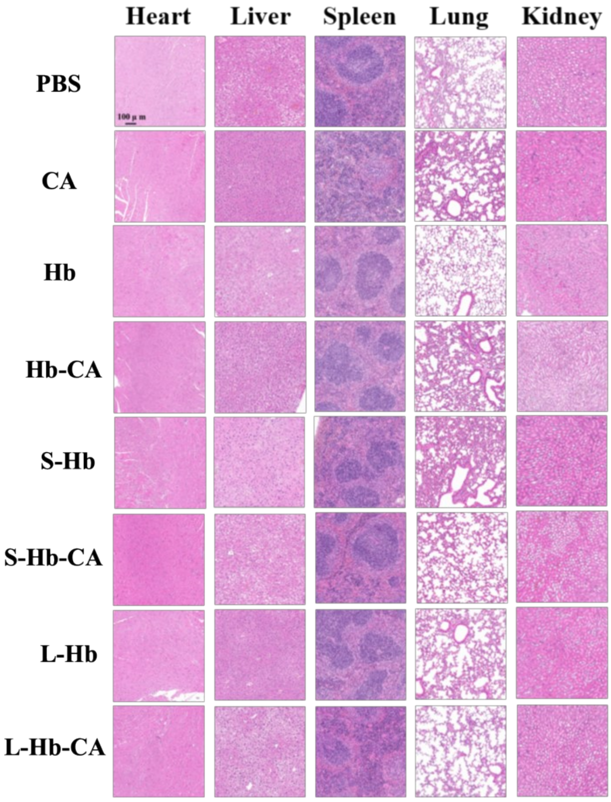

Fig. S10 H&E staining of major organs 10 days after treatment.

2.9 ROS Scavenging Mechanism in Wound Tissues

ROS immunofluorescence staining (Fig. S11) further elucidated the underlying mechanism of accelerated wound healing. On day 3, the PBS group exhibited dense and intense red fluorescence signals, indicating significant ROS accumulation in the wound bed. In contrast, the red fluorescence intensity in the L-Hb-CA group decreased sharply from the early stage of treatment, with only minimal signals observed by day 10. These results demonstrate that L-Hb-CA, through its exceptional ROS scavenging capacity, effectively preserves the mitochondrial function of fibroblasts, thereby enhancing collagen synthesis and tissue repair performance.

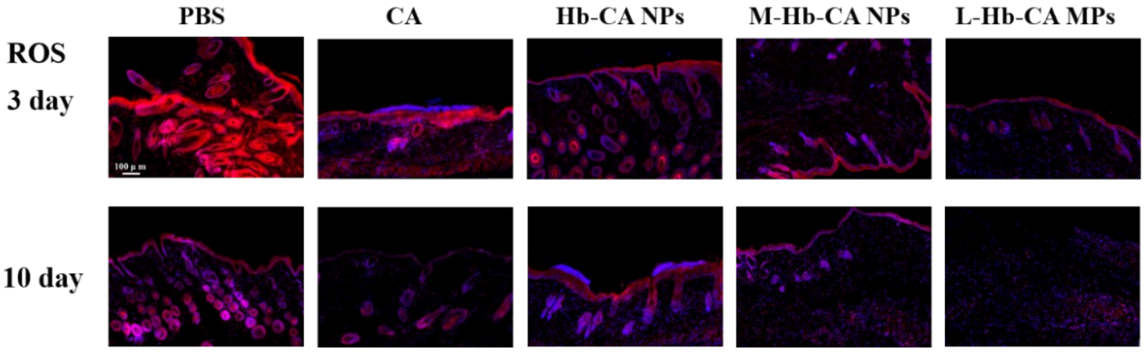

Fig. S11 *In vivo* ROS scavenging performance in wound tissues. Representative immunofluorescence images of ROS (red) in regenerated skin tissues at day 3 and day 10 post-treatment. Scale bar = 100 μm.